Detection of Ice Hydrometeor Alignment Using an Airborne W-band Polarimetric Radar

J. GALLOWAY, A. PAZMANY, J. MEAD, AND R. E. MCINTOSH

Microwave Remote Sensing Laboratory, University of Massachusetts, Amherst, Massachusetts

D. LEON, J. FRENCH, R. KELLY, AND G. VALI

Department of Atmospheric Science, University of Wyoming, Laramie, Wyoming

(Manuscript received 10 April 1996, in final form 25 July 1996)

ABSTRACT

This paper presents airborne W-band polarimetric radar measurements at horizontal and vertical incidence on ice clouds using a 95-GHz radar on the University of Wyoming King Air research aircraft. Coincident, in situ measurements from probes on the King Air make it possible to interpret polarimetric results in terms of hydrometeor composition, phase, and orientation. One of the key polarimetric measurements recently added to those possible with the W-band radar data system is the copolar correlation coefficient ρ_{HV}. A discussion of the relation between cloud scattering properties and ρ_{HV} covers a test for isotropy of the distribution of observed hydrometeors in the plane of polarization and qualitative evaluation of the possible impact of Mie (resonant) scattering on ρ_{HV} measurements made at W band. Prior measurements of ρ_{HV} at S band and Ku band are compared with the W-band results. The technique used to measure ρ_{HV}, including the real-time and postprocessing steps required, is explained, with a discussion of the expected measurement error for the magnitude and phase of ρ_{HV}.

Cloud data presented include melting-layer observations at vertical incidence, observation of a convective snow cell at vertical incidence, and observations of needle crystals at both horizontal and vertical incidence. The melting layer observations provide a consistency check for the measurements of ρ_{HV} and linear depolarization ratio (LDR) at W band through the test for isotropy. The vertical incidence measurements of a convective snow cell displayed significant mean orientation of the hydrometeors observed in the features evident in Z_{DR} and the phase of ρ_{HV}. Data taken on needle crystals provided clear indication of particle alignment in the measurements of Z_{DR} and LDR for the horizontal incidence case and equally clear indication of a lack of orientation for the vertical incidence case.

1. Introduction

The development of an airborne 95-GHz system to address the need for finescale cloud measurements began in 1990 with field experiments at the University of Wyoming Elk Mountain Observatory (Pazmany et al. 1994a). The first experimental use of the radar system aboard the University of Wyoming King Air took place during the fall of 1992 (Pazmany et al. 1994b; Vali et al. 1995), when the W-band radar retrieved data from clouds to provide estimates of Z_{eHH}, Z_{DR}, and linear depolarization ratio (LDR) along with pulse-pair estimates of Doppler velocity and spectral width. This application of the combination of the 95-GHz radar and the aircraft cloud physics sensors established the feasibility and utility of W-band polarimetric radar for finescale measurements of clouds from a small research aircraft.

The Winter Icing and Storms Project field studies of 1994 (WISP94) continued a study of upslope and wave cloud microphysics and dynamics in the Colorado Front Range area begun in 1990 and 1991 (Rasmussen et al. 1992). The University of Massachusetts (UMass) Microwave Remote Sensing Lab (MIRSL) and University of Wyoming teams contributed in situ particle measurements and 95-GHz polarimetric radar measurements of clouds from the University of Wyoming King Air research aircraft. The results from this experiment were intended to extend current understanding of the application of W-band polarimetric radar techniques to the study of ice cloud microphysics from airborne platforms. Topics of interest included precipitation initiation, cloud entrainment, and water phase transitions in winter storms.

Extensions of the capability of this system to measure the copolar correlation coefficient as well as the full Doppler spectrum using a real-time FFT were un-

Corresponding author address: John C. Galloway, Microwave Remote Sensing Lab. 20, University of Massachusetts, 102 Knowles Eng. Bldg., Amherst, MA 01003.
E-mail: galloway@alex.ecs.umass.edu

dertaken and completed before WISP94. This required the addition of the cross correlation between linear horizontal (H) and vertical (V) return signals to the parameters processed in real time. Simultaneous sampling of copolar return from both H and V transmit pulses given the current system hardware is not possible, so the correlation must be formed between copolar samples separated by a single pulse repetition period T_s. Normalization of this cross correlation to the signal powers in H and V and correction for decorrelation due to hydrometeor movement during the sampling interval results in an estimate of the copolar correlation coefficient ρ_{HV}. The meteorological applications of ρ_{HV} are detailed in Doviak and Zrnić (1993) and have been demonstrated with measurements from S-band and Ku-band radar systems, both airborne and ground based (Zrnić et al. 1994).

This paper discusses detection of significant ice hydrometeor alignment with the 95-GHz radar. Section 2 discusses the known relations between a cloud's composition and ρ_{HV} established using S-band and Ku-band systems and addresses some of the difficulties of making such measurements using a 3-mm wavelength radar. The section 3 details the real-time processing and postprocessing necessary to produce the final data products, Z_{eHH}, Z_{DR}, LDR, ρ_{HV}, and Doppler velocity. Section 4 includes case studies of polarimetric measurements made during field experiments in 1992 and 1994. Section 5 provides an assessment of the use of a W-band radar in studies of particle orientation in ice clouds.

2. Relations between the copolar correlation coefficient and cloud composition

a. Fundamental relation

The relation between ρ_{HV} and the elements of the scattering matrix for particles in a given volume may be found in (Zrnić et al. 1994; Jameson 1989)

$$\rho_{HV} = \frac{\langle |S_{HHi}|\ |S_{VVi}| e^{j(\phi_{Hi}-\phi_{Vi})}\rangle}{(\langle |S_{HHi}|^2\rangle\langle |S_{VVi}|^2\rangle)^{1/2}}, \tag{1}$$

where S_{HHi} and S_{VVi} are the complex amplitudes relating H and V backscattered fields to H and V incident fields, respectively, for the ith particle in the volume; and ϕ_{Hi} and ϕ_{Vi} are the cumulative propagation and backscattered phases for the received copolar fields. The expectation indicated is taken over all the particles in a given volume. The quantities of interest from this correlation coefficient include its magnitude $|\rho_{HV}|$ and phase $\arg(\rho_{HV})$.

The phase of the copolar correlation coefficient is, in general, composed of differential propagation and backscattered phase δ. When hydrometeors present different propagation properties to H and V polarized fields, the specific differential phase K_{DP} is the parameter used to characterize the propagation phase difference with range. Specific differential phase is defined as the difference between the H and V propagation constants (k_h and k_v), which are simply additions to the free-space propagation constant, $k_0 = 2\pi/\lambda$, when hydrometeors are present in a given volume (Doviak and Zrnić 1993). Since K_{DP} depends inversely on wavelength for scattering in the Rayleigh region, values of K_{DP} from Rayleigh scatterers as measured at W band will be approximately 30 times larger than similar measurements made at S band. For hydrometeors in the resonance scattering region, however, K_{DP} no longer depends inversely on wavelength. The presence of resonance region scatterers also brings about differential backscattered phase δ, the difference between the phases of S_{HH} and S_{VV}, which also increases the phase difference between H and V polarized fields measured for a particular range. Therefore, any measurement of $\arg(\rho_{HV})$ at W band may include both components: propagation and backscatter phase differences. The sum of differential propagation phase and δ is often denoted Φ_{DP}, defined by (Doviak and Zrnić 1993)

$$\Phi_{\mathrm{DP}}(r_0) = 2\int_0^{r_0} [k_h(r) - k_v(r)]\, dr + \delta(r_0). \tag{2}$$

The magnitude of the copolar correlation coefficient decreases with variation between the H and V backscattered return signal on the basis of hydrometeor size distribution, shape and/or orientation distribution, differential backscatter phase distribution, and mixtures of different kinds of hydrometeors (Balakrishnan and Zrnić 1990). Other investigators have demonstrated that $|\rho_{HV}|$ will decrease due to changes in axial ratio, canting and drop oscillations in rain (Doviak and Zrnić 1993). These measurements have principally been characterized for lower frequencies (S and Ku bands) and used to identify regions in which hail and rain are mixed (Balakrishnan and Zrnić 1990) or to characterize the melting layer (Zrnić et al. 1994).

A relationship exists between LDR and $|\rho_{HV}|$ that forces the following to be true for scatterers that are isotropically distributed in the plane of polarization (Mead et al. 1991):

$$|\rho_{HV}| = 1 - 2(10^{\mathrm{LDR}/10}), \tag{3}$$

where $\arg(\rho_{HV})$ is zero and LDR is the linear depolarization ratio defined by

$$\mathrm{LDR} = 10 \log_{10}\left(\frac{\langle |S_{HV}|^2\rangle}{\langle |S_{VV}|^2\rangle}\right). \tag{4}$$

When it is known that the particles in a given region should provide isotropic backscatter in the plane of polarization, this relation provides a check for self-consistency in the radar data. In particular, observations of hydrometeors at vertical incidence are expected to obey this relation in the absence of forces inducing alignment, such as electrification.

b. Notable effects at 95 GHz

Backscatter from ice clouds frequently falls into the resonance region characterized by $0.1\lambda <$ particle size $< 10\lambda$ at W band. Resonance region backscatter may produce appreciable differential backscatter phase for aligned, nonspherical particles in addition to the propagation phase difference (Oguchi 1973). If the distribution of backscattered and forward-scattered phases is broad for the observed volume, the effect in the ensemble over the volume will be to decrease the value of $|\rho_{HV}|$. Therefore, particles large enough to fall in the resonance region may cause additional ambiguity in the interpretation of a decrease in $|\rho_{HV}|$ from unity (Zrnić et al. 1993; Jameson 1989).

In general, K_{DP} will be nonzero whenever particles are anisotropically distributed in the plane of polarization. Calculation of K_{DP} at 95 GHz is complicated by the fact that resonance region scattering is accompanied by differential backscatter phase in addition to differential propagation phase. This biases the estimate of K_{DP}, which might otherwise be calculated as the range derivative of $\arg(\rho_{HV})$. For the purposes of this discussion concerning ρ_{HV} measurements at W band, the term $\arg(\rho_{HV})$ will be used to include both differential propagation and backscatter phase to avoid any possible confusion with the prior definitions of Φ_{DP} and K_{DP} used for lower frequency systems.

3. Polarimetric measurement description

a. Sampling and real-time processing

A real-time DSP-based system sampled and processed the radar return provided by the 95-GHz radar in order to reduce the data rate to manageable proportions. The processing system was configured to key the radar with four pulses separated by 50 μs in the following transmit polarization sequence: *VVHH*, repeated every 2 ms. The analog-to-digital (A/D) converters sampling at 5 MHz provided 100 range gates spaced 30 m apart. Given the nominal airspeed of the King Air (100 m s^{-1}) and an antenna diameter of 0.3 m, this provided 100 independent, sampled range profiles of the complex return signal for use in forming running averages of the desired products: copolar powers P_{HH} and P_{VV}, crosspolar power P_{HV}, copolar correlation coefficient ρ_{HV}, and pulse-pair correlation ρ_{HH}. These products were formed approximately three times per second and stored to disk. This sample rate produced pixels that are about 30 m along track at the flight line (90-m range) and about 66 m along track at the farthest range (2.97-km range). Statistics describing the radar system's performance during WISP94 are given in Table 1. A discussion of the data processing in real-time involved in measurements made in 1992 may be found along with a more detailed discussion of the radar system's characteristics in Pazmany et al. (1994b).

TABLE 1. The 95-GHz radar specifications for WISP94.

Transmit frequency	94.92 GHz
Peak power	1.2 kW
Pulse duration	200 ns (30 m)
Pulse repetition frequency	20 kHz
Antenna diameter	30.5 cm
Antenna beam width	0.7°
Receiver noise figure	11 dB (SSB)
Receiver bandwidth	18 MHz

b. Postprocessing for $|\rho_{HV}|$ and $\arg(\rho_{HV})$

Postflight processing involved estimation of Z_{eHH}, Z_{DR}, LDR, $|\rho_{HV}|$, $\arg(\rho_{HV})$, and K_{DP} from the real-time products; Z_{eHH} and Z_{DR} were calculated in the standard fashion, and LDR was calculated using the procedure described in Pazmany et al. (1994b). The Doppler velocity was measured using the pulse-pair technique as detailed in Doviak and Zrnić (1993). The complex return samples may be labeled V_{pq}, where p refers to the received polarization and q refers to the transmitted polarization. Given the available complex samples, $\hat{\rho}_{HH}(T_s)$, $\hat{\rho}_{HV}(T_s)$, and $|\hat{\rho}_{HV}|$ were estimated as follows:

$$\hat{\rho}_{HH}(T_s) = \frac{N^{-1}\sum_{i=0}^{N-1} V_{HH0i}V^{*}_{HH1i}}{P_{HH}} \tag{5}$$

$$\hat{\rho}_{HV}(T_s) = \frac{N^{-1}\sum_{i=0}^{N-1} V_{HH0i}V^{*}_{VV1i}}{(P_{HH}P_{VV})^{1/2}} \tag{6}$$

$$|\hat{\rho}_{HV}| = \left|\frac{\hat{\rho}_{HV}(T_s)}{\hat{\rho}_{HH}(T_s)}\right|, \tag{7}$$

where the asterisk denotes complex conjugate, $\hat{\rho}_{HH}(T_s)$ and $\hat{\rho}_{HV}(T_s)$ are simply first-lag (50 μs) auto- and cross-correlation estimates, and P_{HH} and P_{VV} are estimates of the copolar power in H and V including receiver noise subtraction. The number of samples N is 100. Correction from single lag to zero lag as accomplished in (7) is detailed in Zrnić et al. (1994) and Mead et al. (1996). The phase of ρ_{HV} was estimated using the phases of $\hat{\rho}_{HV}(T_s)$ and $\hat{\rho}_{HH}(T_s)$. The phase of $\hat{\rho}_{HV}(T_s)$ contains both the Doppler phase shift and $\arg(\rho_{HV})$, while the phase of $\hat{\rho}_{HH}(T_s)$ is determined by Doppler shift alone; therefore, $\arg(\rho_{HV})$ may be calculated as

$$\arg(\hat{\rho}_{HV}) = \arg\left[\frac{\hat{\rho}_{HV}(T_s)}{\hat{\rho}_{HH}(T_s)^{*}}\right]. \tag{8}$$

The range derivative of $\arg(\rho_{HV})$, K_{DP}, was estimated using a procedure detailed in Doviak and Zrnić (1993). Values of K_{DP} were found as the slope taken from a least squares fit to a line using a sliding window of 16 points of $\arg(\rho_{HV})$ along a given range profile to produce a profile of K_{DP} values. The range associated with a given K_{DP} value was taken to be the center of the window.

The standard deviations of $|\hat{\rho}_{HV}|$ and $\arg(\hat{\rho}_{HV})$ as func-

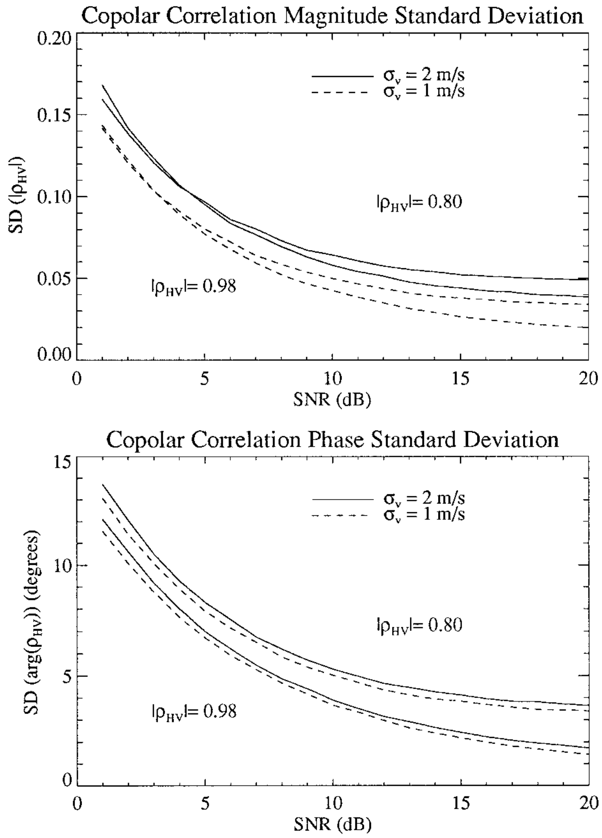

FIG. 1. Plots of standard deviations of $|\hat{\rho}_{HV}|$ and $\arg(\hat{\rho}_{HV})$ vs single-pulse SNR, $\mathrm{SNR}_{HH} = \mathrm{SNR}_{VV}$ assumed. The Z_{eHH} value corresponding to 0-dB single-pulse SNR at 1-km range is -11 dBZ_e.

tions of SNR were determined by a simulation requiring generation of two complex time series with Gaussian spectra of a specified spectral width using the procedure outlined in Chandrasekar et al. (1986). Each simulated value of ρ_{HV} was generated from 100 independent samples of two series 2048 points long. The sampling of the two series was performed in exactly the same manner as the data was actually taken (VVHH samples separated by T_s corresponding to a pulse repetition frequency (PRF) of 20 kHz). The actual values of ρ_{HV} used in the simulation were generated from the V and H receiver samples using (7) and (8). Taking sample standard deviations of 10 000 realizations of the magnitude and phase of the simulated ρ_{HV} values provided measurement standard deviation estimates for specified signal-to-noise ratios (SNR) and spectral widths. Figure 1 shows the dependence of the standard deviations in $|\hat{\rho}_{HV}|$ and $\arg(\hat{\rho}_{HV})$ on single-pulse SNR and spectral width. The expected standard error for single-pulse SNR greater than or equal to 10 dB for Z_{DR} is 0.5 dB as calculated using the formula presented in Sachidananda and Zrnić (1985). The expected standard deviation of the cross-polar power measurements used to calculate LDR may be found in Pazmany et al. (1994b). The variance of K_{DP} (° km^{-1}) may be found in the discussion of calculation of K_{DP} from a linear least squares fit to a line of $\arg(\rho_{HV})$ values (°) found in Doviak and Zrnić (1993). Given that the range window of $\arg(\rho_{HV})$ values used for each estimate of K_{DP} was 480 m (16 gates) long, the standard deviation of K_{DP} was 0.9 times that of $\arg(\rho_{HV})$.

4. Observations

Observations from WISP94 and the fall of 1992 provide examples of the response of Z_{DR}, LDR, $|\hat{\rho}_{HV}|$, and $\arg(\hat{\rho}_{HV})$ to the cloud conditions observed. These include 1) two observations of melting layers (one from nimbostratus in 1992 and the other from an elevated warm air layer in WISP94), 2) observations of needle crystals at horizontal and vertical incidence from WISP94, and 3) observation in a snowstorm of significant particle alignment possibly induced by cloud electrification.

a. Melting-layer cases

A case of well-defined melting band was observed on 31 October 1992 about 200 km northeast of Laramie, Wyoming. Deep nimbostratus formed over an extensive area as a result of a shortwave disturbance. Clouds extended to above 10 km and consisted of distinct generating cells in the upper regions, followed by more uniform regions of ice crystals. Horizontal variability in the cloud was minimal over the 30-km region probed by the aircraft. The flight pattern consisted of a series of passes at decreasing altitudes in a staircase fashion from 7 km to the surface.

Equivalent potential temperature increased with height at an average rate of 1.8 K km^{-1}, confirming the stability of the cloud. The 0°C level was at the 2.5-km altitude, and the temperature at the surface (at 1.5-km altitude) was $+4$°C. Light rain was falling at the surface, consisting of drops to a maximum of 1-mm diameter, and producing rainfall rates between 0.2 and 0.6 mm h^{-1}. Above the melting level, the cloud consisted entirely of ice crystals, except for transient patches of low cloud liquid water content around the 3.5-km altitude. Below 3 km, the air was not fully saturated leading to evaporation of ice crystals falling from above; this decreased the precipitation rate but did not lead to complete evaporation.

The radar data shown in Fig. 2 were obtained during a gradual descent from 1.7 to 1.45 km with the radar beam pointing upward (vertical incidence observation). The horizontal stratification of the reflectivity above 3.5 km is clearly evident; this is the result of wind shear in the regions of generating cells at cloud top. The weak echo region below about 2.5 km is due to the partial evaporation mentioned earlier. The top of the lower echo layer is the 0°C level. Vertical profiles of Z_{eHH}, fall velocity, and LDR appear in Fig. 3. The LDR values measured for this melting layer ranged between -12 and -22 dB. The lower LDR value, -22 dB, represents the minimum LDR measurement possible given the system

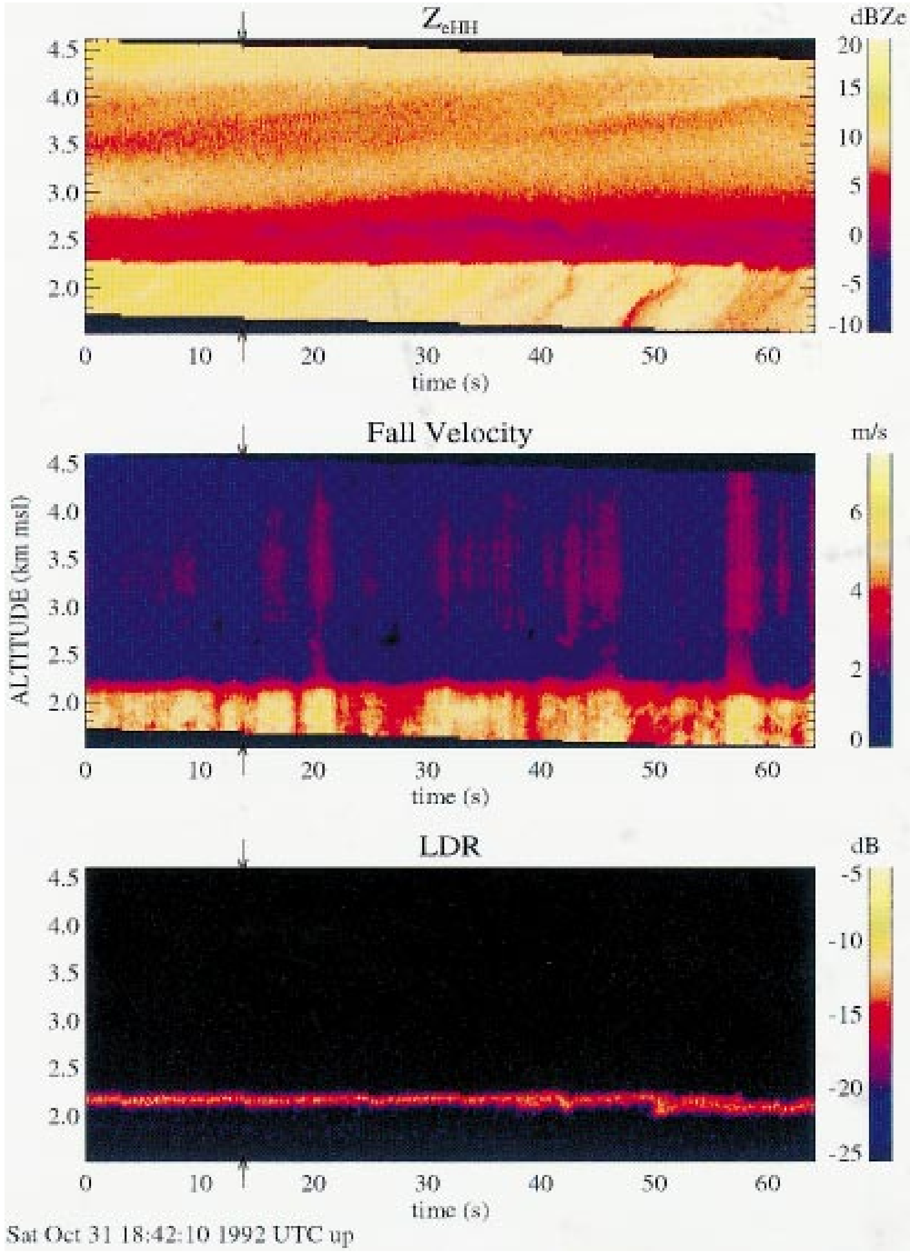

FIG. 2. Images of Z_{eHH}, fall velocity, and LDR from melting layer observed on 31 October 1992. The arrows indicate the location of the profiles plotted in Fig. 3.

polarization isolation and thresholding used to calculate LDR. The values of fall velocity indicated a sharp transition in the hydrometeor fall speed between 2- and 2.2-km altitude. The weak-echo region shows up clearly in the Z_{eHH} profile between the 2.2- and 2.7-km altitudes. The size distributions of crystals and of drops, from above and below the melting level, are shown in Fig. 4.

The characteristics of the melting band on 31 October 1992 were qualitatively similar to other cases reported for observations with longer wavelengths. The detailed observations of hydrometeor shapes and sizes available for this case will allow quantitative comparisons with calculated Z_{eHH} and LDR values when modeling of complex shapes becomes possible and provide a basis for comparisons with other cases of 95-GHz observations. The observed LDR maximum of -12 dB is the strongest such signal we have found so far at this frequency.

During 1992, measurements of $|\rho_{HV}|$ were not possible with the data system then available for use with the W-band radar. Therefore, no comparison was then available between $|\rho_{HV}|$ measurements at S band from the

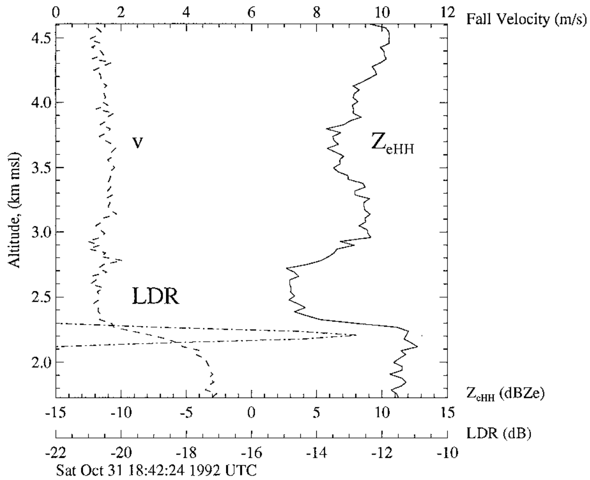

FIG. 3. Vertical profiles of Z_{eHH}, fall velocity, and LDR from melting layer observed on 31 October 1992.

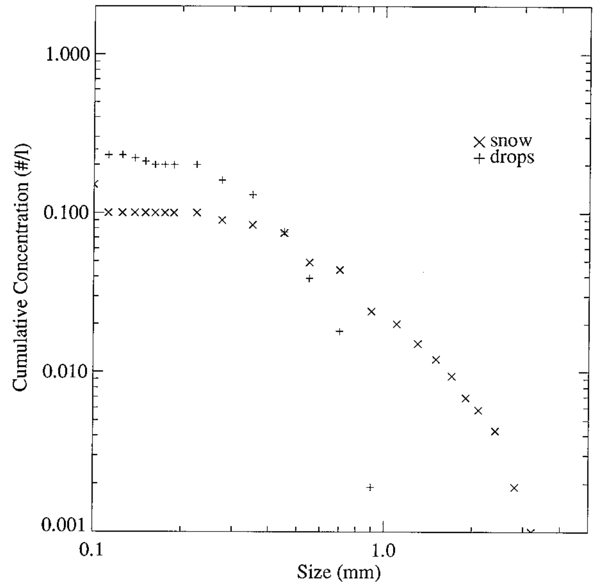

FIG. 4. Cumulative concentration size spectra for observation of a melting layer on 31 October 1992. Spectra for both ice above melting layer and drops below melting layer.

ground and using the W-band airborne radar when viewing a melting band. The measurements of depolarization and $|\rho_{HV}|$ provide a consistency check on the radar data through the use of relation (3) when applied to melting band data. However, that measurement had to wait until the radar data processing system was modified for the WISP94 experiment.

The case of a melting layer from WISP94 provided a means of comparing the observations of $|\rho_{HV}|$ at W band with those of previous investigators. Zrnić et al. (1993, 1994) and Jameson (1989) have examined $|\rho_{HV}|$ from melting layers. Past observations have indicated that $|\rho_{HV}|$ drops sharply at the bottom of a melting layer. Data on a melting layer was taken as the King Air made a missed approach to the Norman, Oklahoma, airport. The aircraft was ascending from 1800 to 2050 m in altitude (-2.8 to -3.7°C), passing through freezing drizzle beneath an elevated layer of warm ($T > 0$°C) air. A sample of the 2D particle images at flight level is shown in Fig. 5.

There is a clear signature of the melting layer between 200 and 600 m above the flight level in the LDR and $|\hat{\rho}_{HV}|$ images (see Fig. 6). Range profiles of Z_{eHH}, LDR, and $|\rho_{HV}|$ at 35.7 s along track (closest to the melting layer) are shown in Fig. 7. The minimum values of $|\hat{\rho}_{HV}|$ attained in the middle of the melting layer are around 0.9, which agrees with data presented in Zrnić et al. (1994) from an airborne Ku-band radar and ground-based S-band radar. Here Z_{eHH} shows some features corresponding to those in LDR and $|\hat{\rho}_{HV}|$, but does not show a bright band as clearly. Figure 8 plots the correspondence between $|\hat{\rho}_{HV}|$ and $1 - 2(10^{\mathrm{LDR}/10})$ along a range profile at the same time. These data are consistent with (3), which follows from the isotropic distribution of the hydrometeors in the plane of polarization in the melting layer.

b. Needle crystals

During two successive radar observations on 6 March 1994, (1848:14–1850:15 UTC and 1851:46–1852:45 UTC), the aircraft passed through crystal populations that were nearly all needles. Samples of the 2DC images from these periods are shown in Fig. 9. These images indicate single needle crystals exceeding 1 mm in size, and aggregates up to 3-mm size.

The first segment of radar observations of needle crystals were horizontal-looking (the pitch varied by less than 2° and the roll varied from -2° to $+2$°). The $|\rho_{HV}|$ and $1 - 2(10^{\mathrm{LDR}/10})$ measurements at the range gate closest to the aircraft probes (90-m range) are summarized in Fig. 10, as histograms of all the points available during this period. The separation between the mean values of $|\rho_{HV}|$ and $1 - 2(10^{\mathrm{LDR}/10})$ of 0.03 is on the order of the standard deviation of $|\rho_{HV}|$. This separation indicates a substantial difference between the two measurements. Therefore, the relation in (3) does not apply to these hydrometeors; the needle crystals

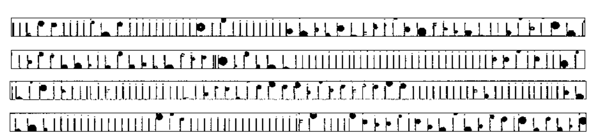

FIG. 5. The 2DC images taken under melting layer observed on 8 March 1994. The time period for the first pair of lines was 2238:40.88–2238:41.54 UTC and that for the second pair was 2239:07.94–2239:08.50 UTC. The vertical extent of each of the four strips of images is 800 μm. It should be kept in mind that these images are a projection of the observed hydrometeor shadows onto a horizontal plane.

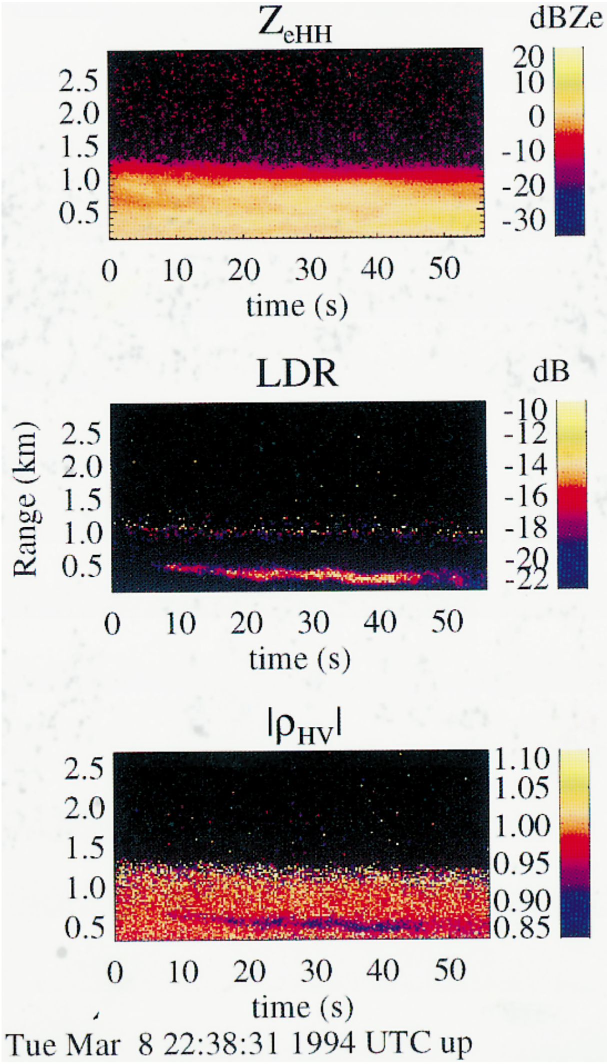

FIG. 6. Images of Z_{eHH}, LDR, and $|\rho_{HV}|$ for melting layer over Norman, Oklahoma.

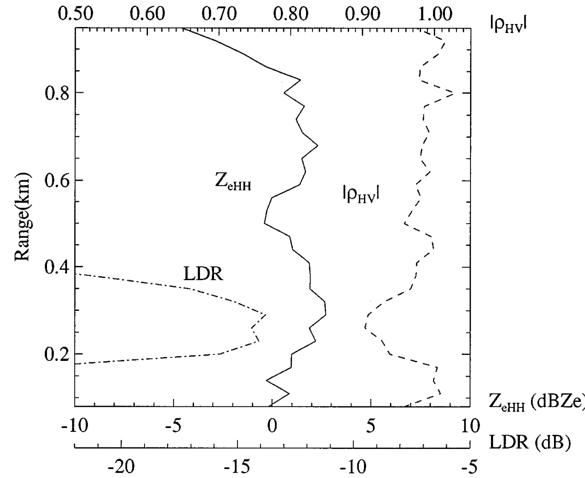

FIG. 7. Plot of LDR, $|\hat{\rho}_{HV}|$, and Z_{eHH} at point of closest approach to melting layer over Norman, Oklahoma.

have a clear preferred orientation in the plane of polarization. Corresponding Z_{DR} values between 2.5 and 5 dB indicate that the needles were dominantly in a horizontal orientation, as expected for horizontal-incidence observation. A population of needle crystals falling with their principal axes aligned parallel to the H axis would not be expected to produce LDR values greater than the system minimum detectable LDR of -22 dB. However, the LDR values between -16 and -10 dB indicate that the hydrometeors took on a range of orientations with respect to the H axis. This range of orientations may have been due to actual motion of the needle crystals or may have been induced by the presence of aggregates of needles.

The second set of needle crystal radar observations was at vertical incidence (the pitch was between 4.4° and 8.8° and the roll was between $-11°$ and 4.5°). Histograms of $|\rho_{HV}|$ and $1 - 2(10^{\mathrm{LDR}/10})$ at the range gate closest to the aircraft probes (90-m range) are shown in Fig. 11. The separation between the mean values of $1 - 2(10^{\mathrm{LDR}/10})$ and $|\rho_{HV}|$ in this case is only 0.009; therefore, these values of $|\rho_{HV}|$ and $1 - 2(10^{\mathrm{LDR}/10})$ appear to satisfy relation (3), which would indicate agreement with the scenario of random orientation of nonspherical particles in the plane of polarization, as expected for needle crystals observed at vertical incidence. The Z_{DR} values along track for this case range from 0 to 1 dB and are centered about 0.3 dB, within a standard error of 0 dB as expected for a vertical incidence observation. The LDR values are between -21 and -13 dB. For these cases, Z_{DR} values have a standard error of around 0.5 dB and LDR values have a standard error of near 1–2 dB.

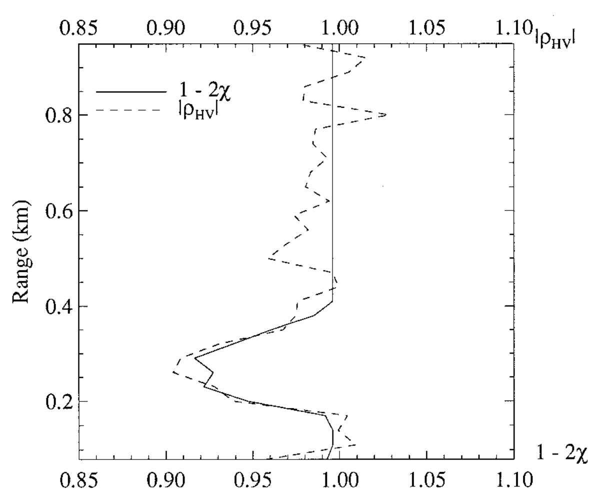

FIG. 8. Plots of $|\hat{\rho}_{HV}|$ and $1 - 2(10^{\mathrm{LDR}/10})$ at same point in time as profiles in Fig. 7 ($\chi = 10^{\mathrm{LDR}/10}$).

FIG. 9. The 2DC images of needle crystals observed by the radar at (a) 1848:21.18–1848:22.64 and 1849:26.4–1849:27.5 UTC and (b) 1851:57.5–1852:00.46 and 1852:22.26–1852:23.9 UTC. The vertical extent of each of the four strips of images is 800 μm.

c. Snowstorm case

Vertical incidence observation of a convective region in a snowstorm over Oklahoma City produced clear features in Z_{DR}, arg($\hat{\rho}_{HV}$), and K_{DP}. The King Air was flying at about 3600-m altitude (−2.5°C). A fall streak appears in the image of Z_{eHH} between 30 and 40 s along track at about the 1.5-km range (see Fig. 12). The most striking features in the other images include an increase in Z_{DR} matching the region just above the fall streak, a rapid increase in arg($\hat{\rho}_{HV}$) with range, and an area of large K_{DP} corresponding to the same region.

Figure 13 shows range profiles of Z_{eHH}, Z_{DR}, arg($\hat{\rho}_{HV}$), and K_{DP} at 42 s along track. The fall streak appears as the larger Z_{eHH} values between 0.9- and 1.3-km range above the aircraft. The peak Z_{DR} values occurred at the top of the streak, along with a distinct change in the slope of arg($\hat{\rho}_{HV}$) with range and a zone of higher K_{DP}. The Z_{DR}, arg($\hat{\rho}_{HV}$), and K_{DP} patterns indicate nonspherical particles with common alignment. At the altitude of the fall streak, the crystals would have been growing at temperatures of about −13°C, that is, in the planar habit growth regime.

The first observations with a polarimetric radar of particle orientation induced by electrostatic fields in a thunderstorm were reported by Hendry and McCormick (1976). These observations, made using a circularly polarized ground-based Ku-band system, included cases in which the ice particles observed were nearly vertical under the influence of the electrostatic field and became randomly oriented just after a lightning strike. Circularly polarized S-band systems have also provided observations of particle orientation induced by electric fields in storms (Metcalf 1995). These S-band observations demonstrated that electrification can bring about mean canting angles of as much as 75°, with a K_{DP} measurement of 0.56° km^{-1}, in a group of ice hydrometeors. This large canting angle could possibly explain the observed responses in arg($\hat{\rho}_{HV}$), K_{DP}, and Z_{DR}, raising the question of whether the observed storm was electrically active.

A lightning strike was detected by the National Severe Storms Laboratory lightning observation network, described in MacGorman and Burgess (1994), between 2025 and 2030 UTC around 10 km east of the observation location. This places the lightning strike between 4 and 9 min after the radar observation (2021 UTC). The horizontal wind as measured by the King Air data system was coming from a bearing of 225° (southwest) at 22 m s^{-1}. Assuming that the wind did not change over the course of that 4–9-min interval, the observed cloud region could have moved between 5 and 12 km. This indicates only that there was significant electrical

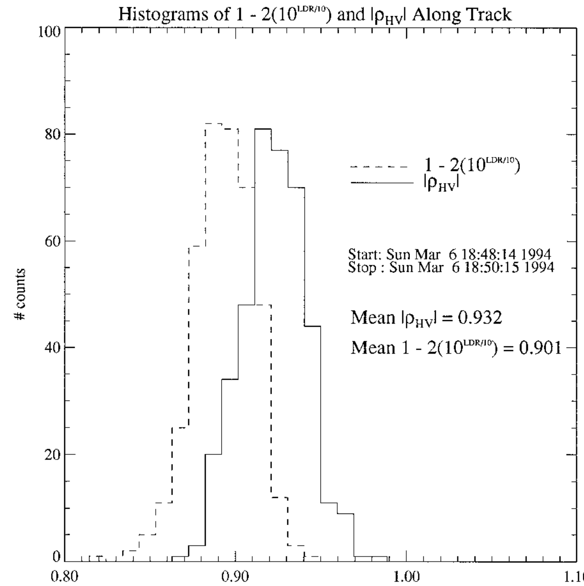

FIG. 10. Histogram of $|\rho_{HV}|$ and $1 - 2(10^{\mathrm{LDR}/10})$ values for observation of needles at horizontal incidence.

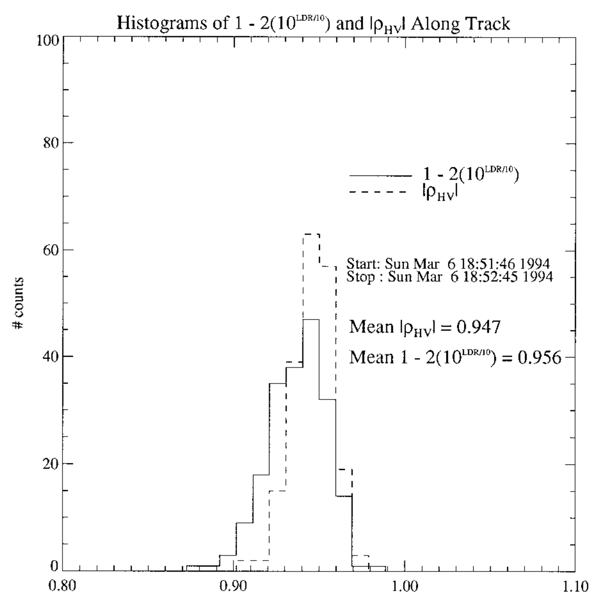

FIG. 11. Histogram of $|\rho_{HV}|$ and $1 - 2(10^{\mathrm{LDR}/10})$ values for observation of needles at vertical incidence.

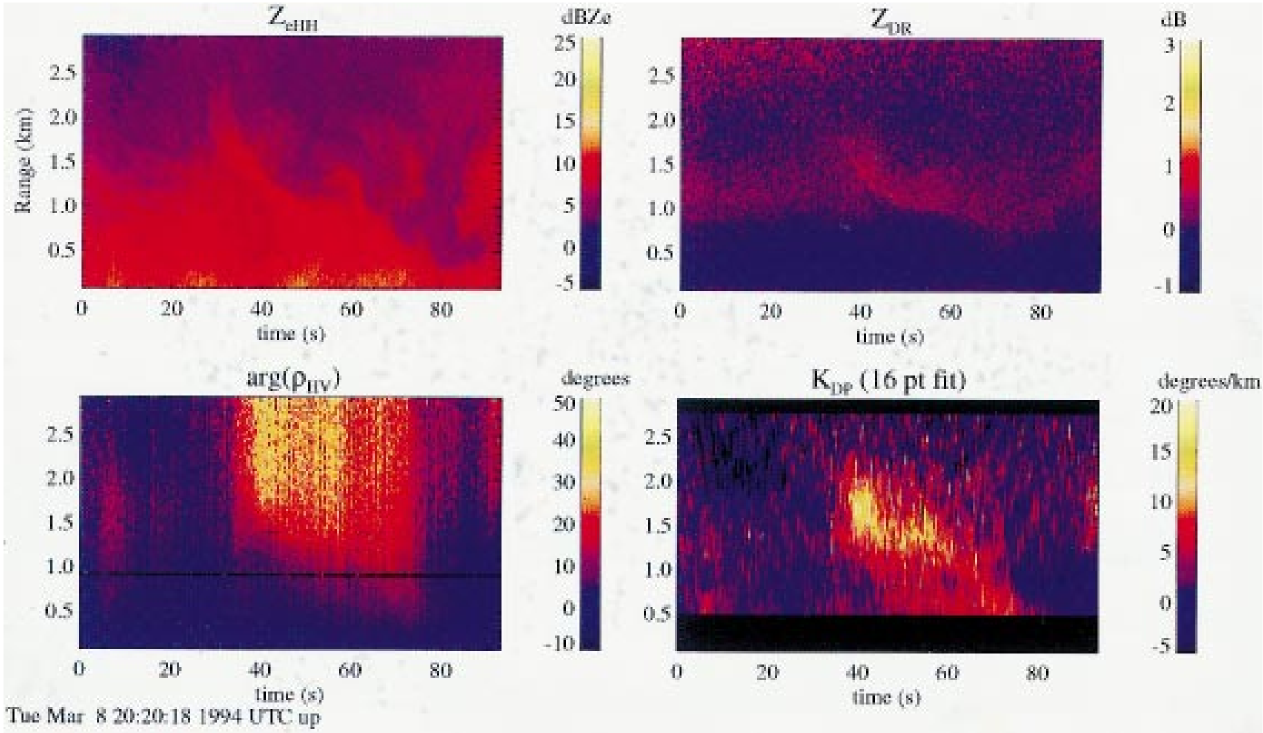

FIG. 12. Images of Z_{eHH}, arg($\hat{\rho}_{HV}$), Z_{DR}, and K_{DP} for observation of a convective snowstorm.

activity in the storm observed and that the storm motion could have accounted for the displacement between the observation and lightning event. It is clear, however, that electrification-induced orientation of hydrometeors cannot be ruled out as a possible explanation of the response seen in Z_{DR}, arg($\hat{\rho}_{HV}$), and K_{DP}.

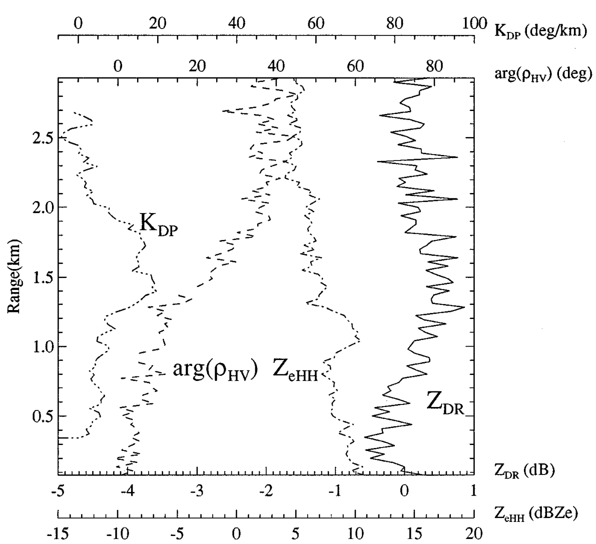

FIG. 13. Plot of Z_{eHH}, Z_{DR}, arg($\hat{\rho}_{HV}$), and K_{DP} at 42 s along track for convective snow cell.

5. Conclusions

The first known airborne polarimetric radar measurements in ice clouds at 95 GHz were made during the field experiments of 1992 and WISP94, with the goal of determining the utility and feasibility of using such 95-GHz radar measurements from the University of Wyoming King Air research aircraft to measure preferred particle orientation in ice clouds. Full use of the in situ measurements provided by the King Air data system along track and the range and alongtrack variation of the polarimetric measurands has been required to form any meaningful interpretation of the radar data. Further work with the airborne system will make use of this unique combination of in situ sampling and polarimetric radar data to form quantitative estimates of particle orientation and shape. This should lead to better information on details of the process of melting, including precipitation rate, degree of riming, and particle sizes.

Since ground-based systems have been measuring melting layers for decades, detecting a melting layer is not a significant addition to applications of radar polarimetry from an airborne platform. The measurement of a melting layer using a W-band radar, however, represents a connection between this state-of-the-art research instrument and operational systems. Having verified that $|\rho_{HV}|$ and LDR measurements of a melting layer are in exact correspondence with prior work and theory for lower-frequency systems, such polarimetric radar data from other targets can be examined with a reasonable hope of finding useful information. Furthermore, the test for isotropic distribution of hydrometeors was verified using melting layer data and provides a tool for testing the same condition for other observations.

Observations of needle crystals at both horizontal and vertical incidence provide polarimetric signatures from a well-understood target with a clearly preferred orientation in the horizontal-looking case and a lack of preferred orientation for the upward-looking case. The test for isotropic distribution of hydrometeors was applied in both cases, and the results agreed with physical intuition about the targets. The presence of sensible LDR in both cases, along with values of Z_{DR} and $|\rho_{HV}|$ characteristic of the medium, provides the possibility of relating the polarimetric signature measured with the radar to the degree of orientation and composition of the hydrometeor population in cases with a single crystal habit present.

Cloud particle orientation and composition changes were indicated by fully polarimetric measurements in a convective region of a snowstorm. The observation of significant differential phase at vertical incidence is the first reported at 95 GHz. Quantitative estimation of the degree of hydrometeor orientation indicated by the differential phase response in this case is complicated by the question of whether the backscatter was substantially in the resonance region. However, regardless of the scattering region, significant mean orientation in the hydrometeors observed was indicated by the Z_{DR}, $\arg(\hat{\rho}_{HV})$, and K_{DP} features.

Acknowledgments. The authors would like to thank Dr. Dusan S. Zrnić of the National Severe Storms Laboratory (NSSL) for his invaluable assistance in interpreting the observation of differential phase at vertical incidence. The assistance of Dr. Irv Watson, also at NSSL, in providing the information from the NSSL lightning detection network was greatly appreciated as well. The measurements discussed in this paper would not have been possible without the support of the following University of Wyoming staff: G. Bershinsky, E. Gasaway, G. Gordon, P. Wechsler, K. Endsley, D. Lukens, and L. Irving. This work was made possible by NSF Grants ATM-9320672 to the University of Massachusetts and ATM-9319907 to the University of Wyoming, administered by Dr. Ron Taylor, program director, Physical Meteorology Program, Atmospheric Sciences Division.

REFERENCES

Balakrishnan, N., and D. Zrnić, 1990: Use of polarization to characterize precipitation and discriminate large hail. *J. Atmos. Sci.,* **47,** 1525–1540.

Chandrasekar, V., V. N. Bringi, and P. J. Brockwell, 1986: Statistical properties of dual-polarized radar signals. Preprints, *23rd Conf. on Radar Meteorology,* Snowmass, CO, Amer. Meteor. Soc., 193–196.

Doviak, R., and D. Zrnić, 1993: *Doppler Radar and Weather Observations.* Academic Press, 576 pp.

Hendry, A., and G. C. McCormick, 1976: Radar observations of the alignment of precipitation particles by electrostatic fields in thunderstorms. *J. Geophys. Res.,* **81** (30), 5353–5357.

Jameson, A. R., 1989: The interpretation and meteorological application of radar backscatter amplitude ratios at linear polarizations. *J. Atmos. Oceanic Technol.,* **6,** 908–919.

MacGorman, D. R., and D. W. Burgess, 1994: Positive cloud-to-ground lightning in tornadic storms and hailstorms. *Mon. Wea. Rev.,* **122,** 1671–1697.

Mead, J. B., P. M. Langlois, P. S. Chang, and R. E. McIntosh, 1991: Polarimetric scattering from natural surfaces at 225 GHz. *IEEE Trans. Antennas Propag.,* **39,** 1405–1411.

——, A. L. Pazmany, P. S. Chang, and R. E. McIntosh, 1996: Comparison of coherent and noncoherent polarimetric radar measurement techniques at 95 GHz. *Radio Sci.,* **31,** 325–333.

Metcalf, J. I., 1995: Radar observations of changing orientations of hydrometeors in thunderstorms. *J. Appl. Meteor.,* **34,** 757–772.

Oguchi, T., 1973: Attenuation and phase rotation of radio waves due to rain: Calculations at 19.3 and 34.8 GHz. *Radio Sci.* **8,** 31–38.

Pazmany, A. L., J. B. Mead, R. E. McIntosh, M. Hervig, R. Kelly, and G. Vali, 1994a: 95-GHz polarimetric radar measurements of orographic cap clouds from the Elk Mountain Wyoming Observatory. *J. Atmos. Oceanic Technol.,* **11,** 140–153.

——, R. E. McIntosh, R. Kelly, and G. Vali, 1994b: An airborne 95 GHz dual-polarized radar for cloud studies. *IEEE Trans. Geosci. Remote Sens.,* **32,** 731–739.

Rasmussen, R., and Coauthors, 1992: Winter icing and storms project. *Bull. Amer. Meteor. Soc.,* **73,** 951–974.

Sachidananda, M., and D. S. Zrnić, 1985: Z_{DR} measurement considerations for a fast scan capability radar. *Radio Sci.,* **20,** 907–922.

Vali, G., R. D. Kelly, A. Pazmany, and R. E. McIntosh, 1995: Airborne radar and in-situ observations of a shallow stratus with drizzle. *Atmos. Res.,* **38,** 361–380.

Zrnić, D., N. Balakrishnan, C. Ziegler, V. Bringi, K. Aydin, and T. Matejka, 1993: Polarimetric signatures in the stratiform region of a mesoscale convective system. *J. Appl. Meteor.,* **32,** 678–693.

——, ——, A. Ryzhkov, and S. Durden, 1994: Use of copolar correlation coefficient for probing precipitation at nearly vertical incidence. *IEEE Trans. Geosci. Remote Sens.,* **32,** 740–748.